A THERMODYNAMICALLY-CONSISTENT MODEL FOR ATP PRODUCTION IN MITOCHONDRIA

GUADALUPE C. GARCIA[1], THOMAS M. BARTOL[1], TERRENCE J.SEJNOWSKI[1], AND PADMINI RANGAMANI[2,*]

ABSTRACT. Life is based on energy conversion. In the nervous system, in particular, significant amounts of energy are needed to maintain synaptic transmission and homeostasis. To a large extent, neurons depend on oxidative phosphorylation in mitochondria to meet their high energy demand. To develop a comprehensive understanding of the metabolic demands in neuronal signaling, accurate models of ATP production in mitochondria are required. Here, we present a thermodynamically-consistent model of ATP production in mitochondria based on previous work [1, 2, 3, 4]. The significant improvement of the model is that the reaction rate constants are set, so detailed balance is satisfied. Moreover, using thermodynamic considerations, the dependence of the reaction rate constants on membrane potential, pH, and substrate concentrations are explicitly provided. These constraints assure us the model is physically-plausible. We provide a complete and detailed derivation of ATP production in mitochondria. Furthermore, we explore different parameter regimes to understand in which conditions ATP production or its export are the limiting step in making ATP available in the cytosol. The outcomes reveal that, under physiological conditions, ATP production is the limiting step and not its export. Finally, we analyze the portion of the total volume taken up by the membranes and study the functional effect this compression can have on the availability of ATP in the cytosol. A compression of approximately 50% of the intermembrane space or the matrix can increase the amount of ATP in the cytosol by 2-6%. This model lays the foundation for future studies of the internal mitochondrial physiology and metabolism in neurons using Monte-Carlo techniques to simulate the biochemical interactions that take place in the mitochondrial compartments.

Date: August 16, 2022.

[1] Computational Neurobiology Laboratory, Salk Institute for Biological Studies, La Jolla CA, 92037.

[2] Department of Mechanical and Aerospace Engineering, University of California, San Diego, La Jolla CA 92093.

*To whom correspondence should be addressed. e-mail: prangamani@ucsd.edu.

CONTENTS

Abbreviations 3

1. Introduction 3

2. Model development 5

2.1. Model for ATP synthase 5

2.2. Model for ATP/ADP translocator (ANT) 11

2.3. Molecular VDAC Model 17

2.4. Metabolite buffers 17

3. Simulation methods 18

4. Mathematical analysis and results 18

4.1. Steady-state flux analysis for the model components 18

4.2. Under physiological conditions, ATP production is the limiting step for cytosolic ATP availability. 19

4.3. Half of the IMS is taken up by the membrane volumes 21

4.4. The compression of the IMS speeds up reactions and makes more ATP available in the cytosol 24

5. Discussion 25

6. Acknowledgments 28

References 29

ABBREVIATIONS

ATP	adenosine triphosphate
ADP	adenine diphosphate
OM	outer membrane
IM	inner membrane
ETC	electron-transport chain
Pi	inorganic phosphate
CM	cristae membrane
IMS	intermembrane space
VDAC	voltage dependent anion channel
ANT	adenine nucleotide translocator
ODEs	ordinary differential equations

1. INTRODUCTION

Energy conversion is at the core of cellular function. Finding efficient strategies to transduce energy has driven the evolution of cells and organisms. In eukaryotic cells, respiration occurs in specialized organelles, known as mitochondria, where metabolic substrates are converted to adenosine triphosphate (ATP), the energy currency of cells [5]. Mitochondrial architecture provides an efficient framework for cellular respiration. It is composed of two distinct membranes: the outer membrane (OM) and the inner membrane (IM). The internal lipid bilayer is used to generate an electrochemical proton gradient, through a series of electron carriers known as the electron-transport chain (ETC) (Figure 1). The energy stored in this gradient drives the synthesis of ATP from adenine diphosphate (ADP) and inorganic phosphate (Pi), through a multiprotein complex, ATP synthase [6]. The outer membrane plays a central role in controlling the flow of molecules from and to the interior of mitochondria. Although it forms a barrier to large molecules, it contains a large number of transport proteins, voltage dependent anion channel (VDAC) [7], that allow the passage of small metabolites and ions. In contrast, the IM is impermeable to molecules; carrier proteins and ion channels are required for molecules to cross this barrier. One of the most relevant carriers is the adenine nucleotide translocator (ANT), which transports ATP and ADP to and from the matrix, the internal region encapsulated by the IM (Figure 1). Overall, this is a membrane-based process that relies on the lipid bilayer of mitochondria to generate the energy required for ATP synthesis.

The importance of ATP production by mitochondria means that reliable mathematical formulations are necessary to build a quantitative framework. To that effect, there have been many mathematical models developed to describe the processes involved in ATP production [1, 2, 8, 9, 10]. Pietrobon and Caplan [1] developed a proton pump model, that can be interpreted as a respiration-driven proton pump or as a model of ATP synthase [2]. Later on, Magnus and Keizer [2] assembled different components and built a

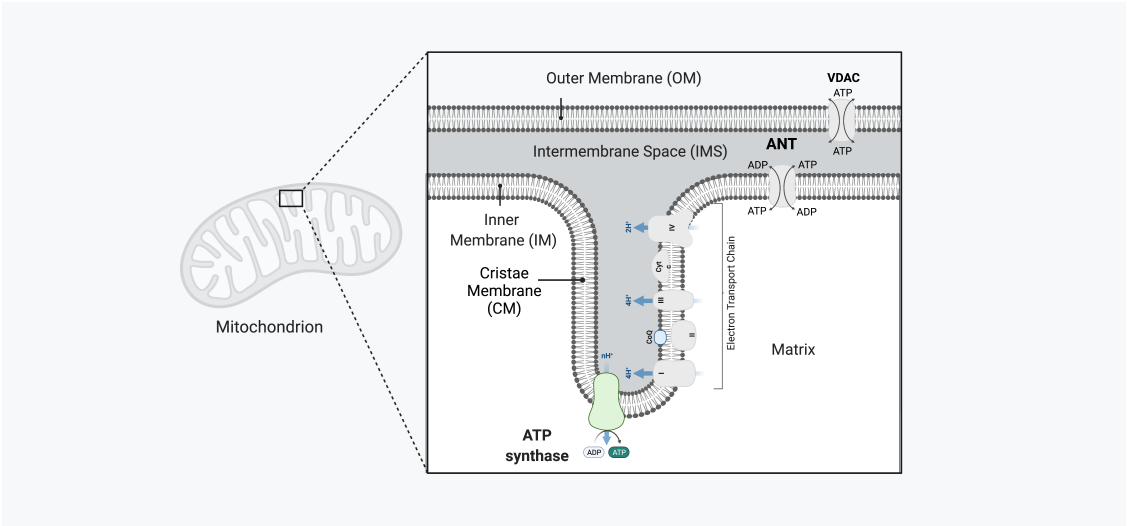

FIGURE 1. Schematic representation of a mitochondrion with its functional components and compartments. The outer membrane (OM) is the external lipid bilayer that interfaces the cytosol. The inner membrane (IM) encapsulates the matrix, it is composed of two functionally distinct regions, the inner boundary membrane (IBM) (in close opposition to the OM) and the cristae membrane (CM). The cristae membrane (CM) is the place where the protein complexes from the electron-transport chain (ETC) reside. At the apex of the CM and along the tubular cristae ATP synthases are allocated. Through these protein complexes, ATP is synthesized in the matrix. ATP is further transported from the matrix through adenine nucleotide translocators (ANTs) to the intermembrane space (IMS)—the space between the two membranes— to finally cross the OM at voltage dependent anion channel (VDAC), to reach the cytosol.

steady-state model of ATP production in mitochondria, which several other models are based on [8, 10, 9]. However, they did not explicitly show how the thermodynamic constraints were imposed to the system [1]. Here, to ensure the model is thermodynamically-consistent, we imposed detailed balance constraints to the reaction rate constants. We further incorporated a more precise model of ADP/ATP translocation in mitochondria [3]. Our goal was to develop a reaction-based model that can be directly implemented to run spatial or non-spatial simulations.

With the developed model, we answered the following questions: under physiological conditions, what limits the amount of ATP that reaches the cytosol? Is it the rate of production of ATP or is it the rate of ATP export from the mitochondria to the cytosol? What portion of the volumes is taken up by the membranes and what are the functional

[1]These calculations were reported to be in a Ph.D. thesis we could not get access [11]. Recently, we found part of these calculations were included in another PhD thesis [12]

implications of the compression of the IMS or the matrix compartment? To answer these questions, we developed a thermodynamically-consistent model of ATP production in mitochondria – i.e. a physically-plausible model. Our criteria for thermodynamic consistency was, for each cycle in the model, to calculate the thermodynamic forces [13] and to equate this to the ratio of the forward to backward reaction rate constants. In this manner, we verified detailed balance was satisfied for the conditions considered. Furthermore, we calculated the dependence of the reaction rate constants on the membrane potential, pH, ATP, ADP, and Pi concentrations. We conducted simulations of this model using ordinary differential equations (ODEs); although simpler, this approach is informed with detailed structural calculations of surface areas and volumes from a realistic 3D reconstruction [4]. The outcomes reveal that, under physiological conditions, ATP production in the matrix is the limiting factor. We also found that the intermembrane space (IMS) is compressed by 50% due to the membrane thickness and this compression can increase the amount of ATP in the cytosol by 6%. This work lays the foundation for future studies of structure-function relationships in these critical organelles, using Monte-Carlo techniques to simulate the biochemical interactions that take place in the mitochondrial compartments.

2. Model development

The model presented here is based on previous work [1, 2, 3, 4]. Our efforts were focused on assembling a thermodynamically-consistent model [13], and explicitly highlighting the dependence of the reaction rates constants on the membrane potential, pH, ATP, ADP, and Pi concentration.

2.1. **Model for ATP synthase.** The ATP synthase model is grounded on the work of Pietrobon and Caplan [1]. The kinetic model consists of a membrane protein –represented as E– that transports protons (H^+) from the IMS to the matrix. The protein can be in six states represented in Figure 2A. A clockwise cycle starting in state 6 (E^{-3}) represents the binding of 3 protons from the IMS (transition 6 $\rightarrow$ 5 in Figure 2B), transport of the protons to the matrix (state 5 $\rightarrow$ 4), binding of ADP and $\mathrm{P_i}$ (state 4 $\rightarrow$ 3) and subsequent synthesis of ATP (state 3 $\rightarrow$ 2), followed by unbinding of the protons in the matrix (state 2 $\rightarrow$ 1). We considered a constant proton concentration inside the IMS and the matrix, and the ATP and ADP concentration as variables. The list of the reactions is given in Table 1 and the model parameters are given in Table 2. We next explain how some kinetic parameters depend on the membrane potential, the proton concentration, and the phosphate concentration.

2.1.1. *Thermodynamic constraints.* Thermodynamic constrains are imposed on the rate constants of the system. At an arbitrary steady-state, the product of the first-order (or pseudo-first order) rate constants around a cycle κ in the positive direction ($\prod_{\kappa^+}$) divided by the product of the rate constants in the negative direction ($\prod_{\kappa^-}$) is related to net thermodynamic forces in the following manner [13]:

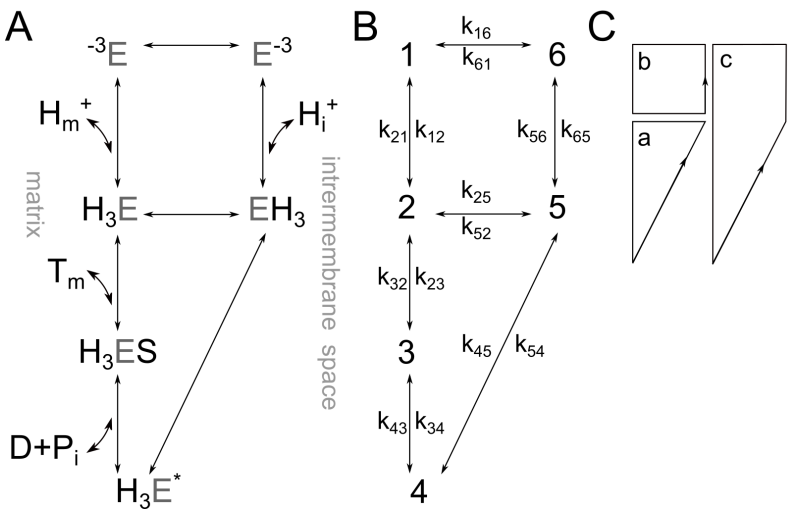

FIGURE 2. Kinetic diagram of the ATP synthase model [1]. (A) The model consists of six states, representing different protein configurations. ATP molecules are represented as T, ADP molecules as D, Phosphate as $\mathrm{P_i}$, ATP synthase as E, and H^+ as protons. The model considers the binding of ATP and ADP from the matrix and the IMS. States toward the matrix are on the left and oriented toward the IMS space are on the right. (B) Each state has associated a number from 1 to 6. A clockwise cycle, starting from state 6 (E^{-3}) corresponds to the binding of 3 protons from the IMS (transition 6 $\rightarrow$ 5), followed by their transport to the matrix (transition 5 $\rightarrow$ 4) and subsequent binding of ADP and $\mathrm{P_i}$ (transition 4 $\rightarrow$ 3), to the synthesis of ATP (transition 3 $\rightarrow$ 2), and unbinding of 3 protons in the matrix (transition 2 $\rightarrow$ 1). The subscripts in state 1 and 6 correspond with a negative charged cavity facing the matrix and intermembrane space. Each transition has an associated rate constants $\mathrm{k_{ij}}$. In some cases $\mathrm{k_{ij}}$ depends on the membrane potential, proton concentration, or phosphate concentration. The list of all the reactions is in Table 1 and the list of parameters in Table 2. (C) The cycles are considered positive in the counter-clockwise direction, and named a, b, and c.

$$\frac{\prod_{\kappa^+}}{\prod_{\kappa^-}} = \mathrm{e}^{(\frac{\chi}{\mathrm{RT}})} = \mathrm{e}^{(\frac{\Delta \mathrm{G}_\kappa}{\mathrm{RT}})}, \tag{2.1}$$

where χ is the net thermodynamic force, $\Delta\mathrm{G}_\kappa$ is the difference in Gibbs free energy per mole of substance (i.e. the chemical potential) in the cycle κ, R is the universal gas constant and T is the absolute temperature. At thermodynamic equilibrium, and in absence of a potential difference between the membranes, the $\Delta\mathrm{G}$ in the cycle is zero. This leads to a ratio of forward rate constants to backward rate constants equal to one (Eqs 2.1), also known as detailed balance.

List of Reactions for the ATP synthase model
$^{-3}\mathrm{E} + 3\mathrm{H}^{+}_{\mathrm{m}} \underset{k_{21}}{\overset{k_{12}}{\rightleftharpoons}} \mathrm{H_3E}$
$\mathrm{H_3E} + \mathrm{T}^{+}_{\mathrm{m}} \underset{k_{32}}{\overset{k_{23}}{\rightleftharpoons}} \mathrm{H_3ES}$
$\mathrm{H_3ES} \underset{k_{43}}{\overset{k_{34}}{\rightleftharpoons}} \mathrm{H_3E^*} + \mathrm{D_m}$
$\mathrm{H_3E^*} \underset{k_{54}}{\overset{k_{45}}{\rightleftharpoons}} \mathrm{EH_3}$
$\mathrm{EH_3} \underset{k_{65}}{\overset{k_{56}}{\rightleftharpoons}} \mathrm{E}^{-3} + \mathrm{H}^{+}_{\mathrm{i}}$
$\mathrm{E}^{-3} \underset{k_{16}}{\overset{k_{61}}{\rightleftharpoons}} {}^{-3}E$

TABLE 1. List of reactions for the ATP synthase model.

Starting with the shortest cycle, **b** in the diagram (Figure 2C) we obtain:

$$\frac{\prod_{\mathrm{b}+}}{\prod_{\mathrm{b}-}} = \mathrm{e}^{(\frac{\chi}{\mathrm{RT}})} = \mathrm{e}^{(\frac{\Delta \mathrm{G_b}}{\mathrm{RT}})}. \tag{2.2}$$

Replacing the rate constants in the cycle we get:

$$\frac{\mathrm{k_{12}k_{25}k_{56}k_{61}}}{\mathrm{k_{21}k_{52}k_{65}k_{16}}} = \mathrm{K_{12}K_{25}K_{56}K_{61}}, \tag{2.3}$$

where $\mathrm{K_{ij}}$ are the equilibrium constants of the transitions from state i to state j. The equilibrium constants are given by [14]:

$$\mathrm{K_{ij}} = \frac{\mathrm{k_{ij}}}{\mathrm{k_{ji}}} = \mathrm{e}^{\frac{\mathrm{G_i - G_j}}{\mathrm{RT}}}, \tag{2.4}$$

where $\mathrm{G_i}$ and $\mathrm{G_j}$ are the Gibbs free energy per mole for species in states i and j respectively. The equilibrium constant for the transition from state 1 to 2, where three protons bind from the matrix side, is equal to:

$$\mathrm{K_{12}} = \frac{\mathrm{k_{12}}}{\mathrm{k_{21}}} = \mathrm{e}^{\frac{\mathrm{G_1 - G_2}}{\mathrm{RT}}}, \tag{2.5}$$

where $\mathrm{G_1}$ is the Gibbs free energy per mole of three protons in the matrix and $\mathrm{G_2}$ the energy of the protons bound to the membrane. These are given by [14]:

$$\mathrm{G_1} = \mathrm{G_1^o} + 3\mathrm{F}\Psi_1 + 3\mathrm{RT}\ln([\mathrm{H}^{+}_{\mathrm{m}}]),\ \mathrm{G_2} = \mathrm{G_2^o} + 3\mathrm{F}\Psi_2, \tag{2.6}$$

where $\mathrm{G_1^o}$ and $\mathrm{G_1^o}$ are the standard free energy per mole. Here Ψ_1 is the bulk potential at the matrix, Ψ_2 is the phase boundary potential at the surface of the inner membrane, and F is the Faraday's constant. Replacing Eq. 2.6 in Eq. 2.5 we arrive at:

$$\frac{k_{12}}{k_{21}} = e^{(\frac{G_1^o - G_2^o}{RT})} e^{(\frac{-3F\Delta\Psi_b^{in}}{RT})} [H_m^+]^3, \tag{2.7}$$

where $\Delta\Psi_b^{in} = \Psi_2 - \Psi_1$ is the phase-boundary potential (the difference between the bulk potential and the potential at the surface of the membrane, see Figure 3), and $[H_m^+]$ is the proton concentration in the matrix. We define $k_{ij,0}$ as the rate constants at zero potential difference and k_{ij}^* as the rate constants independent of the concentrations; we arrive at:

$$\frac{k_{12}}{k_{21}} = \frac{k_{12}^*}{k_{21,0}} e^{(\frac{-3F\Delta\Psi_b^{in}}{RT})} [H_m^+]^3. \tag{2.8}$$

Following the original model [1], we assign the effect of the phase-boundary potentials to the unbinding rate constant k_{21}, and proton concentration to the binding rate constant k_{12}:

$$k_{21} = k_{21,0} e^{(\frac{3F\Delta\Psi_b^{in}}{RT})},\ k_{12} = k_{12}^* [H_m^+]^3. \tag{2.9}$$

We take a similar approach for the transition $6 \rightarrow 5$, where three protons bind from the IMS to the inner membrane. The Gibbs energy per mole for the protons in the IMS (G_6) and bound to the membrane (G_5) are:

$$G_6 = G_6^o + 3F\Psi_4 + 3RT\ln([H_i^+]),\ G_5 = G_5^o + 3F\Psi_3. \tag{2.10}$$

Replacing Eq. 2.10 in Eq. 2.4 we arrive at:

$$K_{65} = \frac{k_{65}}{k_{56}} = e^{(\frac{G_6^o - G_5^o}{RT})} e^{(\frac{-3F\Delta\Psi_b^{ex}}{RT})} [H_i^+]^3, \tag{2.11}$$

where $\Delta\Psi_b^{ex} = \Psi_4 - \Psi_3$ is the phase-boundary potential from the IMS, and H_i^+ is the proton concentration in the IMS.

As before, we can rewrite Eq. 2.11 with the rate constant at zero potential difference and the rate constant independent of the concentration as:

$$\frac{k_{65}}{k_{56}} = \frac{k_{65}^*}{k_{56,0}} e^{(\frac{-3F\Delta\Psi_b^{ex}}{RT})} [H_i^+]^3. \tag{2.12}$$

The effect of the phase-boundary potentials is assigned to the unbinding rate constants k_{56}, and the proton concentration to the binding rate constant k_{65} and we obtain:

$$k_{56} = k_{56,0} e^{(\frac{3F\Delta\Psi_b^{ex}}{RT})},\ k_{65} = k_{65}^* [H_i^+]^3. \tag{2.13}$$

The transition from state $1 \rightarrow 6$ involves the movement of the negatively charged proton biding site from the matrix to the IMS. Therefore the Gibbs free energy for this transition can be written as:

$$\mathrm{G_1 = G_1^o - 3F\Psi_2,\ G_6 = G_6^o - 3F\Psi_3.} \tag{2.14}$$

Here, Ψ_2 and Ψ_3 are the potentials at the respective membrane surfaces (Figure 3). Replacing in Eq. 2.4 we arrive at:

$$\mathrm{K_{16} = \frac{k_{16}}{k_{61}} = e^{(\frac{G_1^o - G_6^o}{RT})} e^{(\frac{3F\Delta\Psi_m}{RT})},} \tag{2.15}$$

where $\Delta\Psi_\mathrm{m} = \Psi_3 - \Psi_2$. As before, replacing with the rate constants at zero membrane potential difference we reach:

$$\mathrm{\frac{k_{16}}{k_{61}} = \frac{k_{16,0}}{k_{61,0}} e^{(\frac{3F\Delta\Psi_m}{RT})}.} \tag{2.16}$$

Following the original model [1], we considered a symmetrical Eyring barrier [15], with this assumption the individual rate constants can be written as:

$$\mathrm{k_{16} = k_{16,0} e^{(\frac{3F\Delta\Psi_m}{2RT})},\ k_{61} = k_{61,0} e^{(\frac{-3F\Delta\Psi_m}{2RT})}.} \tag{2.17}$$

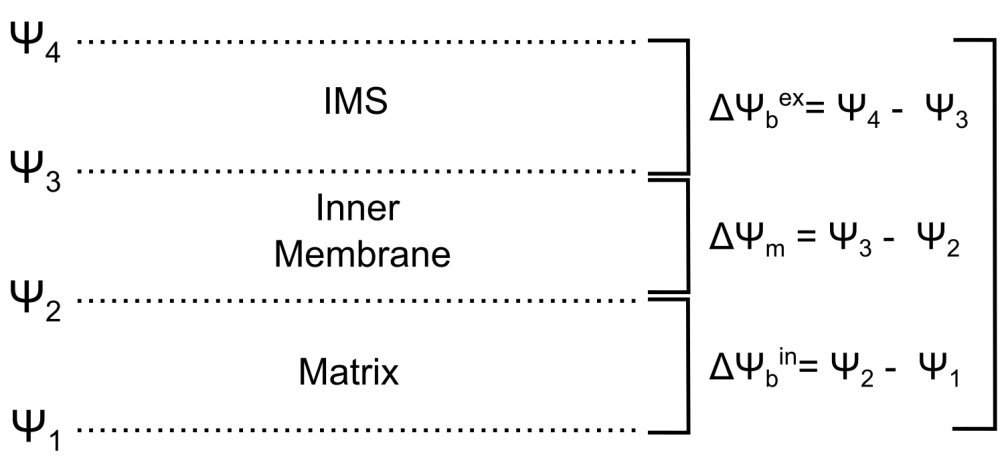

FIGURE 3. Membrane potential considered in the ATP synthase model by Pietrobon and Caplan [1]. $\Delta\Psi = \Psi_4 - \Psi_1$ is the electrical potential difference between the matrix and IMS (or cytosol), $\Delta\Psi_m$ is the electrical potential difference across the membrane, $\Delta\Psi_\mathrm{b}^\mathrm{in}$ and $\Delta\Psi_\mathrm{b}^\mathrm{ex}$ are the phase-boundary potentials.

Substituting the equilibrium rate constants calculated above in Eqs. 2.3 we arrive at:

$$\frac{k_{12}k_{25}k_{56}k_{61}}{k_{21}k_{52}k_{65}k_{16}} = \frac{k^*_{12}}{k_{21,0}} e^{(\frac{-3F\Delta\Psi_b^{in}}{RT})} [H^+_m]^3 \frac{k_{25}}{k_{52}} \frac{k_{56,0}}{k^*_{65}} e^{(\frac{3F\Delta\Psi_b^{ex}}{RT})} [H^+_i]^{-3} \frac{k_{61,0}}{k_{16,0}} e^{(\frac{-3F\Delta\Psi_m}{RT})}. \quad (2.18)$$

At thermodynamic equilibrium, detailed balance impose an additional constraint to the rate constants:

$$\frac{k^*_{12}k_{25}k_{56,0}k_{61,0}}{k_{21,0}k_{52}k^*_{65}k_{16,0}} = 1, \quad (2.19)$$

which yields:

$$\frac{\prod_{b^+}}{\prod_{b^-}} = e^{\frac{-3F(\Delta\Psi_m - \Delta\Psi_b^{ex} + \Delta\Psi_b^{in})}{RT}} \frac{[H^+_m]^3}{[H^+_i]^3} = e^{(\frac{-3F\Delta p}{RT})}. \quad (2.20)$$

Here Δp is the proton motive force:

$$\Delta p = \Delta\Psi - 2.303\,\frac{RT}{F}\Delta pH, \quad (2.21)$$

where $\Delta\Psi$ is the total potential difference across the matrix and the IMS, and ΔpH is the pH difference across the IMS and the matrix ($\Delta pH = pH_i - pH_m$). Similarly for the cycle **a** (Figure 2C) we obtain:

$$\frac{\prod_{a^+}}{\prod_{a^-}} = \frac{k_{23}k_{34}k_{45}k_{52}}{k_{32}k_{43}k_{54}k_{25}} = e^{\frac{\chi_a}{RT}}, \quad (2.22)$$

where χ_a is the thermodynamic force given by:

$$\chi_a = RT\ \ln(K\frac{[ATP]}{[ADP][Pi]}), \quad (2.23)$$

where K is the equilibrium constant of the ATP hydrolysis reaction. At equilibrium, we arrive at:

$$\frac{k_{23}k_{34}k_{45}k_{52}}{k_{32}k_{43}k_{54}k_{25}} = 1. \quad (2.24)$$

This yields:

$$\frac{k^*_{23}k_{34}k_{45}k_{52}}{k_{32}k^*_{43}k_{54}k_{25}} = K, \quad (2.25)$$

imposing further constraints on the rate constants. Finally, for the longest cycle **c**, the thermodynamic force is the sum of forces for cycles **b** and **a**:

$$\Delta G_c = \chi_a - 3F\Delta p = RT\ \ln(K\frac{[ATP]}{[ADP][Pi]}) - 3F(\Delta\Psi - 2.303\,\frac{RT}{F}\Delta pH). \quad (2.26)$$

As before the product of the reaction rate constants relates to the thermodynamic forces in the following manner:

$$\frac{\prod_{c^+}}{\prod_{c^-}} = \frac{k_{23}k_{34}k_{45}k_{52}}{k_{32}k_{43}k_{54}k_{25}} = e^{\frac{\chi_a}{RT}} e^{\frac{-3F\Delta p}{RT}}, \tag{2.27}$$

which at equilibrium can be expressed as:

$$\frac{k^*_{23}k_{34}k_{45}k_{52}}{k_{32}k^*_{43}k_{54}k_{25}} = Ke^{\frac{-3F\Delta p}{RT}}, \tag{2.28}$$

imposing further constraints on the rate constants.

We use the chemical reactions and rate constants presented above to implement the system using compartmental ODEs. As a result of our calculations, the system of ODEs for the ATP synthase model is given by:

$$\begin{aligned}
\frac{dE^{-3}}{dt} &= -k_{65}\,E^{-3} + k_{56}\,EH_3 + k_{16}\,{}^{-3}E - k_{61}\,E^{-3},\\
\frac{d\,{}^{-3}E}{dt} &= -k_{16}\,{}^{-3}E + k_{61}\,E^{-3} - k_{12}\,{}^{-3}E + k_{21}\,H_3E,\\
\frac{dH_3E^*}{dt} &= -k_{45}\,H_3E^* + k_{54}\,EH_3 + k_{34}\,H_3ES - k_{43}\,H_3E^*\,D_m,\\
\frac{dH_3ES}{dt} &= k_{43}\,D_m\,H_3E^* - k_{34}\,H_3ES + k_{23}\,H_3E\,T_m - k_{32}\,H_3ES,\\
\frac{dH_3E}{dt} &= -k_{23}\,H_3E\,T_m + k_{32}\,H_3ES - k_{25}\,H_3E + k_{52}\,EH_3 + k_{12}\,{}^{-3}E - k_{21}\,H_3E.
\end{aligned} \tag{2.29}$$

where variables E^{-3},${}^{-3}E$, etc, are the number of molecules in the different states. The rate constants of the bimolecular reactions have been normalized to have proper units to compute the number of particles, i.e. $k = \frac{k'}{N_A V}$, where k' represents the constants given in Table 2, N_A is the Avogadro's number, and V represents the volume. The volume is either the volume of the matrix or the IMS depending on where the specific reaction occurs (see Simulations Methods section). These five differential equations describe the dynamic of the ATP synthase model. The dynamic of the missing state EH_3 can be deduced, since the total number of proteins is a conserved quantity (E_{tot}), leading to the conservation expression $E^{-3} + EH_3 + H_3E + H_3ES + H_3E^* + {}^{-3}E = E_{tot}$.

2.2. **Model for ATP/ADP translocator (ANT).** The ANT model is based on the work of Metelkin et al. [3]. It is composed of 11 states and 20 bidirectional transitions. The kinetic diagram is shown in Figure 4. The free protein (L) can bound molecules from the matrix (on the right) or IMS side (on the left), forming a triple molecular state (YLX), where Y and X represent ATP or ADP. State YLX can transition to state XLY exporting

Parameter	Definition	Value	Unit	Reference
F	Faraday's constant	9.649×10^{4}	$C\,mol^{-1}$	[16]
R	Universal gas constant	8.315	$J\,mol^{-1}\,K^{-1}$	[16]
pH_m	Matrix pH	7.6		[2]
pH_c	Cristae pH	7.2		[2]
[Pi]	Phosphate concentration	20	mM	[1]
T	Temperature	310	K	
K	Equilibrium constant	1.71×10^{6}	M	[1]
$\Delta\psi$	Membrane potential	180	mV	[1]
$\Delta\psi_{B,i}$	Phase boundary potential	–50	mV	[1]
$\Delta\psi_{B,M}$	Phase boundary potential	0	mV	[1]
$k_{61,0}$	Rate constants at 0 mV	4.98×10^{7}	s^{-1}	[1]
$k_{16,0}$	Rate constants at 0 mV	1×10^{2}	s^{-1}	[1]
$k_{56,0}$	Rate constants at 0 mV	2.75×10^{5}	s^{-1}	[1]
$k_{21,0}$	Rate constants at 0 mV	40	s^{-1}	[1]
k^*_{43}	Rate constants (independent of the concentration)	1×10^{8}	$M^{-2}\,s^{-1}$	[1]
k^*_{12}	Rate constants (independent of the concentration)	6.33×10^{24}	$M^{-3}\,s^{-1}$	[1]
k^*_{65}	Rate constants (independent of the concentration)	1.58×10^{25}	$M^{-3}\,s^{-1}$	[1]
k^*_{23}	Rate constants (independent of the concentration)	5×10^{6}	$M^{-1}\,s^{-1}$	[1]
k_{54}	Rate constant	1×10^{2}	s^{-1}	[1]
k_{32}	Rate constant	5×10^{3}	s^{-1}	[1]
k_{34}	Rate constant	100	s^{-1}	[1]
k_{45}	Rate constant	100	s^{-1}	[1]
k_{56}	Rate constant	1000	s^{-1}	[1]
k_{25}	Rate constant	5.85×10^{-30}	s^{-1}	[1]
k_{52}	Rate constant	1×10^{-20}	s^{-1}	[1]
k_{43}	Rate constant (concentration dependent)	2×10^{6}	$M^{-1}\,s^{-1}$	[1]
k_{12}	Rate constants (concentration dependent)	25	s^{-1}	[1]
k_{65}	Rate constants (concentration dependent)	3969	s^{-1}	[1]
k_{61}	Rate constants at 180 mV	33 989	s^{-1}	[1]
k_{16}	Rate constants at 180 mV	146 516	s^{-1}	[1]
k_{56}	Rate constants at 180 mV	1000	s^{-1}	[1]
k_{21}	Rate constants at 180 mV	40	s^{-1}	[1]

TABLE 2. Parameters for the ATP synthase model.

X to the IMS, and importing Y, following unbinding of the molecules. The productive transition that exports ATP is DLT $\rightarrow$ TLD, the reversal reaction imports ATP to the matrix and exports ADP to the IMS. Two additional states (DLD' and TLT') were

added to track futile translocation (exchange of ADP for ADP and ATP for ATP). Starting from previously fitted flux parameters [3] for ANTs extracted from heart mitochondria [17], we first estimated parameters of the dynamic implementation of the model. With this set of parameters, we qualitatively reproduced the independent data from published work [17, 18]. The rate constant of the model are presented in Tables 4 and 5, and the qualitative reproduction of the experimental data is in Supplementary Figure 1 and Figure 2.

List of Reactions for the ANT model
$T_m + L \underset{k^-_{T_m}}{\overset{k^+_{T_m}}{\longleftrightarrow}} LT$
$D_m + L \underset{k^-_{D_m}}{\overset{k^+_{D_m}}{\longleftrightarrow}} LD$
$T_i + L \underset{k^-_{T_i}}{\overset{k^+_{T_i}}{\longleftrightarrow}} TL$
$D_i + L \underset{k^-_{D_i}}{\overset{k^+_{D_i}}{\longleftrightarrow}} DL$
$T_i + LT \underset{k^-_{T_i}}{\overset{k^+_{T_i}}{\longleftrightarrow}} TLT$
$D_i + LT \underset{k^-_{D_i}}{\overset{k^+_{D_i}}{\longleftrightarrow}} DLT$
$T_i + LD \underset{k^-_{D_i}}{\overset{k^+_{D_i}}{\longleftrightarrow}} TLD$
$D_i + LD \underset{k^-_{D_i}}{\overset{k^+_{D_i}}{\longleftrightarrow}} DLD$
$TLD \xrightarrow{k_{cp}} DLT$
$DLT \xrightarrow{k_p} TLD$
$TLT \xrightarrow{k_t} TLT'$
$TLT' \xrightarrow{k_t} TLT$
$DLD \xrightarrow{k_d} DLD'$
$DLD' \xrightarrow{k_d} DLD$

TABLE 3. List of Reactions for the ANT model.

2.2.1. *Thermodynamic constrains.* As presented in the previous section the parameters of the ANT model are constrained by thermodynamic considerations (Eq. 2.1). If we consider a positive cycle a productive translocation of one ATP from the matrix to the IMS and ADP from the IMS to the matrix (Figure 4C) the product of the rate constants in the positive cycle ($\prod_{\kappa^+}$) divided by the product of the rate constants in the negative cycle ($\prod_{\kappa^-}$) can be written as:

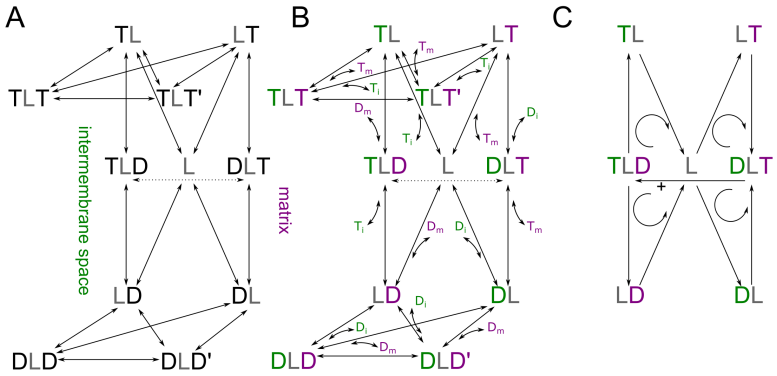

FIGURE 4. Kinetic diagram of the ANT model. (A) The model consists of 11 states, L represents the free protein, and YLX is a triple molecular state with one X molecule bound from the matrix side and one Y molecule bound from the IMS. X and Y represent ATP (T) or ADP (D) molecules. The model has been adapted from previous work [3]. Two additional states (DLD' and TLT') were added to track futile translocation. (B) In this representation, the binding and unbinding of ATP and ADP are explicitly shown, molecules from the IMS side are in green and from the matrix side in purple. (C) The cycles are considered positive going from the matrix to the IMS.

Parameter	Value	Unit
$k^-_{T_m}$	4×10^4	s^{-1}
$k^+_{T_m}$	6.4×10^6	$M^{-1}\,s^{-1}$
$k^-_{T_i}$	200	s^{-1}
$k^+_{T_i}$	4×10^5	$M^{-1}\,s^{-1}$
$k^-_{D_m}$	4×10^4	s^{-1}
$k^+_{D_m}$	4×10^6	$M^{-1}\,s^{-1}$
$k^-_{D_i}$	100	s^{-1}
$k^+_{D_i}$	4×10^6	$M^{-1}\,s^{-1}$
k_p	9.2	s^{-1}
k_{cp}	0.35	s^{-1}
k_d	0.48	s^{-1}
k_t	0.58	s^{-1}
T	310	K
$\Delta\psi$	180	mV

TABLE 4. Parameters for the ANT model at $\Delta\psi = 180\,\mathrm{mV}$.

$$\frac{\prod_{\kappa^+}}{\prod_{\kappa^-}} = \frac{k^+_{T_m}[T_m]k^+_{D_i}[D_i]k_p k^-_{T_i}k_{D_m}}{k^+_{D_m}[D_m]k^+_{T_i}[T_i]k_{cp}k^-_{D_i}k^-_{T_m}}. \tag{2.30}$$

Parameter	Value	Unit
$k^-_{T_m}$	4.4×10^4	s^{-1}
$k^+_{T_m}$	6.4×10^6	M^{-1} s^{-1}
$k^-_{T_i}$	200	s^{-1}
$k^+_{T_i}$	4.8×10^6	M^{-1} s^{-1}
$k^-_{D_m}$	4×10^4	s^{-1}
$k^+_{D_m}$	4×10^6	M^{-1} s^{-1}
$k^-_{D_i}$	100	s^{-1}
$k^+_{D_i}$	4×10^6	M^{-1} s^{-1}
k_p	0.15	s^{-1}
k_{cp}	0.35	s^{-1}
k_d	0.48	s^{-1}
k_t	0.78	s^{-1}
T	310	K
$\Delta\psi$	0	mV

TABLE 5. Parameters for the ANT model at $\Delta\psi = 0\,\mathrm{mV}$.

Here k^- are the backward rate constants and k^+ the forward rate constants for ATP (T) or ADP (D) from the matrix side (m) or the IMS (i), respectively. Replacing with the dissociation constants (the ratio of the backward to forward reaction rates) we arrive at:

$$\frac{\prod_{\kappa^+}}{\prod_{\kappa^-}} = \frac{K_{T_i}K_{D_m}k_p[T_m][D_i]}{K_{D_i}K_{T_m}k_{cp}[D_m][T_i]}, \tag{2.31}$$

where $[D_m]$,$[T_m]$,$[T_i]$ and $[D_i]$ are the concentrations of ADP and ATP in the matrix and IMS respectively. The Gibbs free energy per mole associated with the species before the translocation are:

$$\begin{aligned} G_i &= RT\ln([T_m]) + z_tF\psi_1 + RT\ln([D_i]) + z_DF\psi_4, \\ G_o &= RT\ln([T_i]) + z_tF\psi_4 + RT\ln([D_m]) + z_DF\psi_1, \end{aligned} \tag{2.32}$$

where z_t and z_d are the charge of the ionized forms of ATP and ADP, –4 and –3 respectively. So the difference in Gibbs free energy per mole associated with the translocation of an ionized ATP molecule from the matrix to the IMS, against a concentration gradient and the translocation of an ionized ADP molecule from the matrix to the IMS is equal to:

$$\Delta G = G_i - G_o = RT\ln(\frac{[T_m][D_i]}{[T_i][D_m]}) + F(\psi_4 - \psi_1). \tag{2.33}$$

Combining Eq. 2.31 and Eq. 2.33 we arrive at:

$$\frac{K_{T_i}K_{D_m}k_p[T_m][D_i]}{K_{D_i}K_{T_m}k_{cp}[D_m][T_i]} = e^{\ln\frac{[T_m][D_i]}{[T_i][D_m]}}e^{\frac{F\Delta\psi}{RT}}, \tag{2.34}$$

which reduces to:

$$\frac{K_{T_i} K_{D_m} k_p}{K_{D_i} K_{T_m} k_{cp}} = e^{\frac{F \Delta\psi}{RT}}. \tag{2.35}$$

This equation summarizes the imposing restrictions on the rate constants.

The differential equations for the number of molecules of the ANT model in the different states are:

$$\begin{aligned}
\frac{dL}{dt} &= -(k^+_{T_i} T_i + k^+_{T_m} T_m + k^+_{D_i} D_i + k^+_{D_m} D_m) L + k^-_{T_i} TL + k^-_{T_m} LT + k^-_{D_i} DL + k^-_{D_m} LD, \\
\frac{dTL}{dt} &= k^+_{T_i} T_i L - (k^-_{T_i} + k^+_{D_m} D_m + 2k^+_{T_m} T_m) TL + k^-_{T_m} TLT + k^-_{T_m} TLT' + k^-_{D_m} TLD, \\
\frac{dLT}{dt} &= k^+_{T_m} T_m L - (k^-_{T_m} + k^+_{D_i} D_i + 2k^+_{T_i} T_i) LT + k^-_{T_i} TLT + k^-_{T_i} TLT' + k^-_{D_i} DLT, \\
\frac{dDL}{dt} &= k^+_{D_i} D_i L - (k^-_{D_i} + k^+_{T_m} T_m + k^+_{D_m} D_m) DL + k^-_{D_m} DLD + k^-_{D_m} DLD' + k^-_{T_m} DLT, \\
\frac{dLD}{dt} &= k^+_{D_m} D_m L - (k^-_{D_m} + k^+_{T_i} T_i + k^+_{D_i} D_i) LD + k^-_{D_i} DLD + k^-_{D_i} DLD' + k^-_{T_i} TLD, \\
\frac{dTLD}{dt} &= k^+_{D_m} D_m TL + k^+_{T_i} T_i LD - (k^-_{D_m} + k_{cp}) TLD + k_p DLT - k^-_{T_i} TLD, \\
\frac{dDLD}{dt} &= k^+_{D_i} 0.5 D_i LD + k^+_{D_m} 0.5 D_m DL - (k^-_{D_i} + k^-_{D_m} + k_d) DLD + k_d DLD', \\
\frac{dDLD'}{dt} &= k^+_{D_i} 0.5 D_i LD + k^+_{D_m} 0.5 D_m DL - (k^-_{D_i} + k^-_{D_m} + k_d) DLD' + k_d DLD, \\
\frac{dTLT}{dt} &= k^+_{T_i} 0.5 T_i LT + k^+_{T_m} 0.5 T_m TL - (k^-_{T_i} + k^-_{T_m} + k_t) TLT + k_t TLT', \\
\frac{dTLT'}{dt} &= k^+_{T_i} 0.5 T_i LT + k^+_{T_m} 0.5 T_m TL - (k^-_{T_i} + k^-_{T_m} + k_t) TLT' + k_t TLT.
\end{aligned} \tag{2.36}$$

A vast majority of the models do not consider ATP and ADP concentrations as variables [2, 8]. Because we focused on the local cytosolic environment around a single mitochondrion, we consider ATP and ADP concentrations in the different compartments as variables. To account for their dynamics, we also derived the equations for the number of ATP and ADP molecules in the different compartments:

where D_m is the number of ADP molecules in the matrix, T_m is the number of ATP molecules in the matrix, D_i is the number of ADP molecules in the IMS, T_i is the number of ATP molecules in the IMS, T_{cyto} is the number of ATP molecules in the cytosol, and n_{vdac} is the number of VDACs in the OM.

As before, the rate constants of the bimolecular reactions have been normalized to have proper units to compute the number of particles, i.e. $k = \frac{k'}{N_A * V}$, where k' represents the constants given in Table 4, N_A is the Avogadro's number, and V represents the volume.

$$\frac{dD_m}{dt} = -\left(k^+_{D_m} L + k^+_{D_m} TL + k^+_{D_m} DL + k_{43} H_3E_o\right) D_m + k^-_{D_m} LD + k^-_{D_m} TLD, \quad (2.37)$$
$$+ k^-_{D_m} DLD + k^-_{D_m} DLD' + k_{34} H_3ES,$$
$$\frac{dT_m}{dt} = -\left(k^+_{T_m} L + k^+_{T_m} TL + k^+_{T_m} DL + k_{23} H_3E\right) T_m + k^-_{T_m} LT + k^-_{T_m} DLT, \quad (2.38)$$
$$+ k^-_{T_m} TLT + k^-_{T_m} TLT' + k_{32} H_3ES,$$
$$\frac{dT_i}{dt} = -\left(k^+_{T_i} L + k^+_{T_i} LT + k^+_{T_i} LD + k_p n_{vdac}\right) T_i + k^-_{T_i} TL + k^-_{T_i} TLD, \quad (2.39)$$
$$+ k^-_{T_i} TLT + k^-_{T_i} TLT' + k_p T_{cyto} n_{vdac},$$
$$\frac{dT_{cyto}}{dt} = n_{vdac} k_{vdac} T_c - n_{vdac} k_{vdac} T_{cyto}, \quad (2.40)$$

As for the ATP synthase model, the total number of ANTs is a conserved quantity ($L_{tot} = L + DL + DLD + DLD' + TL + LT + TLT + TLT' + DLT + TLD$).

2.3. **Molecular VDAC Model.** The main mechanism for metabolites to cross the OM is through VDACs. To consider the ATP export from the IMS into the cytosol, we included VDACs. We implemented a rather simple model assuming VDAC proteins interact with ATP molecules and translocate them to the cytosol by the reaction $VDAC + ATP_{IMS} \rightleftharpoons VDAC + ATP_{cyto}$. The lists of parameter values employed is given in Table 6.

Parameter	Value	Unit
k_{vdac}	1×10^6	$M^{-1}\,s^{-1}$
δ	1×10^4	μm^{-2}
n_{vdac}	7.1×10^3	

TABLE 6. Parameters for the VDAC model. The rate constant of the reaction is k_{vdac}, the density of VDAC is δ, and the number of VDAC considered in the simulations is n_{vdac}.

2.4. **Metabolite buffers.** The total concentration of ATP and ADP can be distributed in different compounds or states like ATP^{4-}, ADP^{3-}, $ATPMg^{2-}$, etc. ATP and ADP can react with different cations, be bound, or ionized. The final distributions can be estimated by coefficients representing the fraction of unbound ATP in the matrix or the other compartments. For our model, mitochondrial ADP^{3-} and ATP^{4-} concentrations were estimated analogously to published data [2] as $[ADP]_{m,free} = 0.8\ [ADP]_m$, $[ATP]_{m,free}=[ATP]_m$, $[ATP^{4-}] = 0.05\ [ATP]_{free}$ and $[ADP^{-3}] = 0.45\ [ADP]_{free}$. The initial concentrations of ATP and ADP in the matrix were set to 13 mM and 2 mM, respectively, and to 6.5 mM and 0.1 mM in the IMS and cytosol. In some simulations, these concentrations were kept constant.

3. Simulation methods

The system has a total of 19 equations, and 41 parameters, including chemical rate constants, volumes, and number of proteins. The volumes of the different compartments are listed in Table 7. These values were calculated from a realistic 3D reconstruction of a pre-synaptic mitochondrion [4].

IMS Volume	Matrix Volume	Cyto Volume
0.018 μm^3	0.021 μm^3	0.409 μm^3

Table 7. Volumes of the different compartments considered in the model. These volumes were taken from a realistic 3D reconstruction of a pre-synaptic mitochondrion [4]. The total volume of the organelle is 0.039 μm^3, it is formed by the volume of the IMS (V_{IMS}) and the matrix volume (V_{MA}). The volume of the cytosol is an arbitrary volume (V_{cyto}) set to 0.409 μm^3.

Equations 2.29, 2.37 and 2.40 were integrated using a Radau stiff integrator in PyDSTool [19]. We used BioNetGen [20] to run non-spatial stochastic simulations.

4. Mathematical analysis and results

Before studying the dynamics of the assembled model, we first analyze the behavior of its components separately. In these first simulations, we assume steady-state conditions and keep the ADP and ATP concentrations in the different compartments constant. We then conduct dynamic simulations to understand which is the limiting step in ATP production. Finally, we analyze the volume taken up by the membranes and study its functional consequences on ATP production.

4.1. **Steady-state flux analysis for the model components.** First, we analyze the dependence of the ATP flux on the ADP concentration, membrane potential difference, and pH for the ATP synthase model. The driving forces of the cycle **c** (Figure 2) are the membrane potential, the pH, and the ratio of the ADP and Pi concentration, to the ATP concentration relative to the equilibrium constant (Eq 2.26). For these simulations, the ΔpH is set to -0.4, and the total concentration of adenine nucleotides in the matrix is set to 15 mM. In Figure 5A, we show the ATP net flux through ATP synthases for different concentrations of ADP in the matrix. A positive flux has been taken in the counter-clockwise direction, favoring ATP hydrolysis. We found that at small concentrations of ADP the flux is positive, meaning ATP is hydrolyzed. Increasing the concentration of ADP in the matrix, the ATP flux becomes negative, indicating that ATP synthesis is favored. For concentrations of ADP above 1 mM the flux saturates. Moreover, the driving forces of the cycle also depend on the membrane potential (Eq. 2.26). For a membrane potential above 160 mV the ATP flux is negative, for large concentrations of ADP, but for membrane potential differences below those values ATP is hydrolyzed. Similar results

were obtained for the ATP flux derived by Magnus and Keiser [2], and later modified by Cortassa et al. [8]. Next, we study the dependence of the ATP flux on the pH difference between the matrix and the IMS (Figure 5B). Here, we fixed the pH in the matrix at 7.6 and changed the pH in the IMS. When the pH difference between the matrix and IMS is large, a smaller membrane potential is needed to observe a negative ATP flux, i.e. to synthesized ATP. This is because the proton motive force —the membrane potential minus the difference in pH (Eq. 2.21)— drives the protons to the matrix. The ATP flux also saturates at higher membrane potentials, and in particular, it is almost saturated at 180 mV —the potential considered for the rest of this work. Similar flux dependencies were observed in the past [8].

The driving force of the ANT translocation is the membrane potential and the ratio of $\mathrm{ATP_m/ADP_m}$ in the matrix and $\mathrm{ATP_i/ADP_i}$ in the IMS (Eq. 2.33). Therefore, we study the dependence of the net $\mathrm{ADP_i} - \mathrm{ATP_m}$ flux through ANTs at steady concentrations of ATP and ADP, for different ratios. First, we calculate the net $\mathrm{ADP_i} - \mathrm{ATP_m}$ flux through ANTs for different ratios $\mathrm{ATP_m/ADP_m}$ in the matrix (Figure 6A). Keeping the cytosolic ratio fixed at 65, we varied the $\mathrm{ATP_m/ADP_m}$ ratio. The driving force of the cycle (Eq. 2.33) increases for larger $\mathrm{ATP_m/ADP_m}$ ratios, increasing the net $\mathrm{ADP_i} - \mathrm{ATP_m}$ flux (Figure 6A). The net $\mathrm{ADP_i} - \mathrm{ATP_m}$ flux saturates for ratios $\mathrm{ATP_m/ADP_m}$ closer to the ratio of $\mathrm{ATP_i/ADP_i}$ (Eq. 2.33).

Next, we vary the $\mathrm{ATP_i/ADP_i}$ ratio in the IMS and keep the matrix ratio constant at 6.5. Increasing the $\mathrm{ATP_i/ADP_i}$ ratio decreases the driving force (Eqs. 2.33) at constant $\mathrm{ATP_m/ADP_m}$ ratio. Therefore, the net $\mathrm{ADP_i} - \mathrm{ATP_m}$ flux decreases for larger ratios of $\mathrm{ATP_i/ADP_i}$ (Figure 6B). Moreover, the maximum flux is set by the $\mathrm{ATP_m/ADP_m}$ ratio.

From this analysis we identify that for 2 mM $\mathrm{ADP_m}$, 180 mV membrane potential, and -0.4 $\Delta\mathrm{pH}$, the ATP flux is almost at its maximum absolute value (Figure 5A-B). We use these values for the remainder of this work. Likewise, the initial concentration ratios considered in the rest of this work are $\mathrm{ATP_m/ADP_m} = 6.5$ and $\mathrm{ATP_i/ADP_i} = 65$, from which the $\mathrm{ADP_i} - \mathrm{ATP_m}$ flux through ANTs is almost at its maximal value.

4.2. **Under physiological conditions, ATP production is the limiting step for cytosolic ATP availability.** The amount of ATP in the cytosol depends on the production rate and its export through ANTs and VDACs. Since experimental results suggest the translocation rate constants of the ANT are in the order of 100s per second [21], we explore the impact of fast export through ANTs on the final ATP concentration in the cytosol. We hold the concentration of ADP in the IMS constant (Figure 7A) and change the parameters of the ANT model. Specifically, we change the value of the rate constants $\mathrm{k_p}$, $\mathrm{k_{cp}}$, $\mathrm{k_t}$, and $\mathrm{k_d}$ multiplying them by a factor r, such that detailed balance is still satisfied. We measure the number of ADP and ATP molecules in the matrix (Figure 7B-C), and the number of molecules of ATP in the IMS and cytosol (Figure 7D-E). Faster translocation

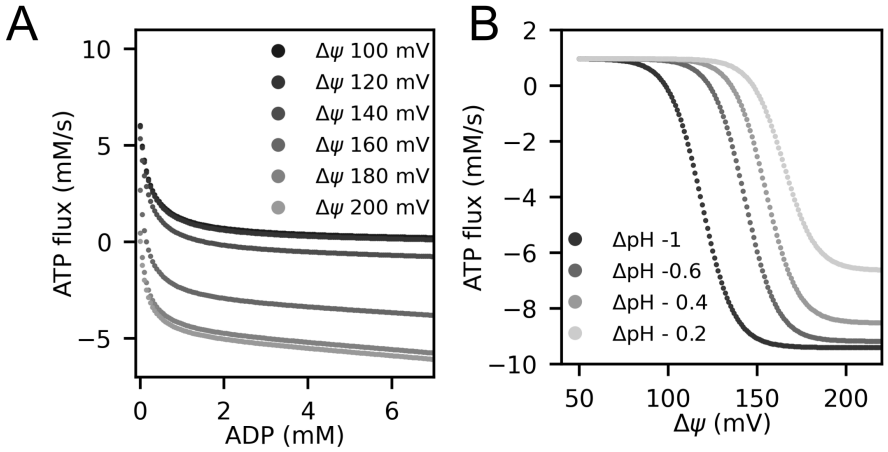

FIGURE 5. ATP synthase steady-state flux analysis. We analyze the dependence on the fluxes through ATP synthases at constant concentrations of adenine nucleotides in the different compartments. We analyze how the flux changes with the driving forces of the cycles (Eqs. 2.26). A) ATP net flux through ATP synthases for different concentrations of ADP in the matrix and different membrane potentials. A counter-clockwise cycle is defined as positive, favoring ATP hydrolysis. For membrane potential above 160 mV, and larger $\mathrm{ADP_m}$ concentrations, ATP is synthesized. B) ATP net flux through ATP synthases for different pH and membrane potentials (for fixed concentrations of adenine nucleotides).

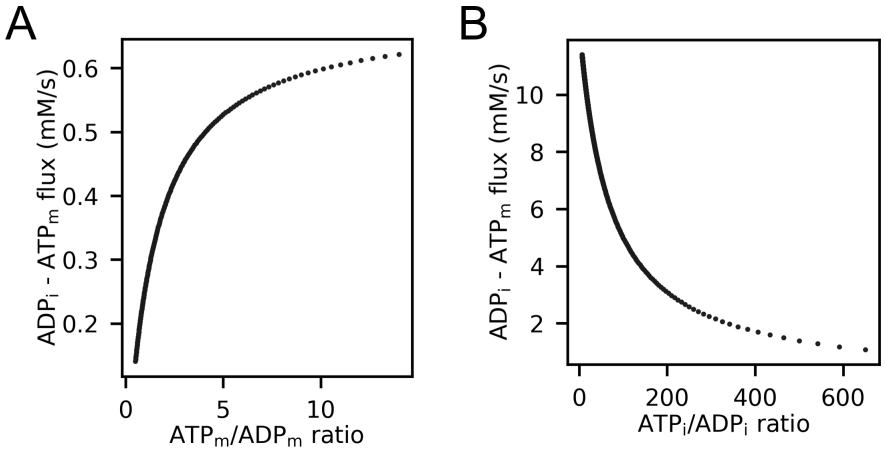

FIGURE 6. ANT steady-state flux analysis. We analyze the dependence on the fluxes through ANTs at constant concentrations of adenine nucleotides in the different compartments. We analyze how the flux changes with the driving forces of the cycles (Eqs. 2.33). A) $\mathrm{ADP_i} - \mathrm{ATP_m}$ net flux through ANTs for different ATP to ADP ratios in the matrix. B) $\mathrm{ADP_i} - \mathrm{ATP_m}$ net flux through ANTs for different ratios of ATP and ADP in the IMS.

allows more ADP to accumulate in the matrix (Figure 7B) and therefore less ATP (Figure 7C), while ATP molecules reach the IMS and the cytosol faster (Figure 7D-E). We further calculate the percentage of the ATP increase relative to the slowest import (Figure 7F). The fastest ANTs (r = 10) exports 26% more ATP molecules than the slowest ones in 1 second. Moreover, the amount of ATP starts to saturate for the fastest ANTs (r = 10). This means even ANTs that are faster cannot overcome the ATP production rate. Thus, the rate limiting step is the ATP production rate, not the export.

In addition to the translocation rate of the ANTs, the number of ANTs to the ATP synthases can influence the export of ATP molecules into the cytosol. Therefore, we next ask how the ratio of ANTs to ATP synthases affects the availability of ATP in the cytosol for the fastest ANTs. We wondered which step limits the number of ATP molecules in the cytosol under these conditions – is it the synthesis of ATP or its translocation through ANTs? As in the previous simulation, the number of ADP molecules in the IMS is constant, assuming unlimited resources (Figure 8A), and we measure the number of ADP, and ATP molecules in the matrix, IMS, and cytosol over time (Figure 8A-E).

The amount of ATP in the cytosol after 1 second starts to saturate when the number of ANTs is twice the number of ATP synthases (Figure 8F). Thus our model predicts that having more ANTs than two times the number of ATP synthases will not have any benefit. If this ratio is bigger than two, the limiting step is the production of ATP. These results are in agreement with experimental conclusions suggesting the ratio of ANTs to ATP synthases is approximately two [22].

Similarly, VDACs can limit the amount of ATP in the cytosol. Therefore, we analyze how the export of ATP through VDACs limits their amount in the cytosol. Considering similar conditions as before (constant concentration of ADP in the IMS, Figure 9), we change the number of VDACs in the OM, and measure the percentage increase of ATP in the cytosol after 1 second (Figure 9F). Having less than 500 VDACs in the OM significantly limits the amount of ATP available in the cytosol. Otherwise, the production of ATP is the limiting step.

Given the density of VDACs in the OM [23] and the surface area of the OM considered [4] (see Methods), the number of VDACs we used in previous simulations is 7100. This number is well above the limiting threshold of 500. Therefore, in all the physiological conditions we considered, the production of ATP is the limiting step.

4.3. **Half of the IMS is taken up by the membrane volumes.** As stated in the methods sections, the values of the surface areas and volumes of all the compartments were obtained from one mitochondrial reconstruction from electron microscopy data [4]. The thickness of the membrane was disregarded in these calculations. However, given the small compartment sizes in mitochondria, we wondered whether considering the membrane thickness would affect the volumes of the various compartments. Considering the membrane thickness as 7 nm [24], we find that the volume of the IMS decreases. In this

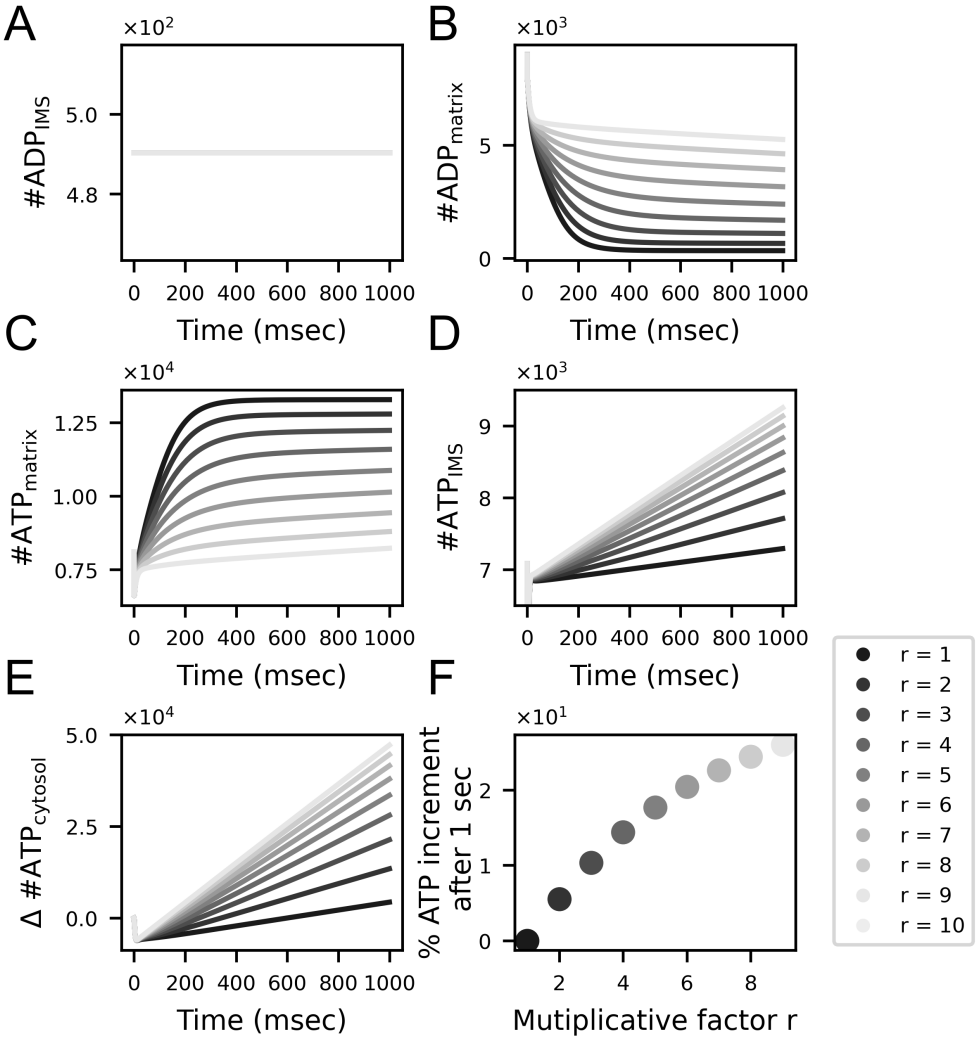

FIGURE 7. Parameter exploration for the ANT model. We change the rate constants of the ANTs, and measure their impact on the dynamics of ATP production. We multiply the rate constants k_p, k_{cp}, k_t, and k_d by a factor r, where r takes values between 1 and 10. (A) Number of ADP molecules measured over time in the IMS. (B) Number of ADP molecules measured over time in the matrix. (C) Number of ATP molecules measured over time in the matrix. (D) Number of ATP molecules measured over time in the IMS. (E) Number of ATP molecules measured over time in the cytosol relative to the initial number of molecules. (F) Percentage increment of the number of ATP molecules in the cytosol after 1 second relative to the slowest ones (r = 1), for all ANTs considered from the slowest (r = 1) ones to the fastest ones (r = 10).

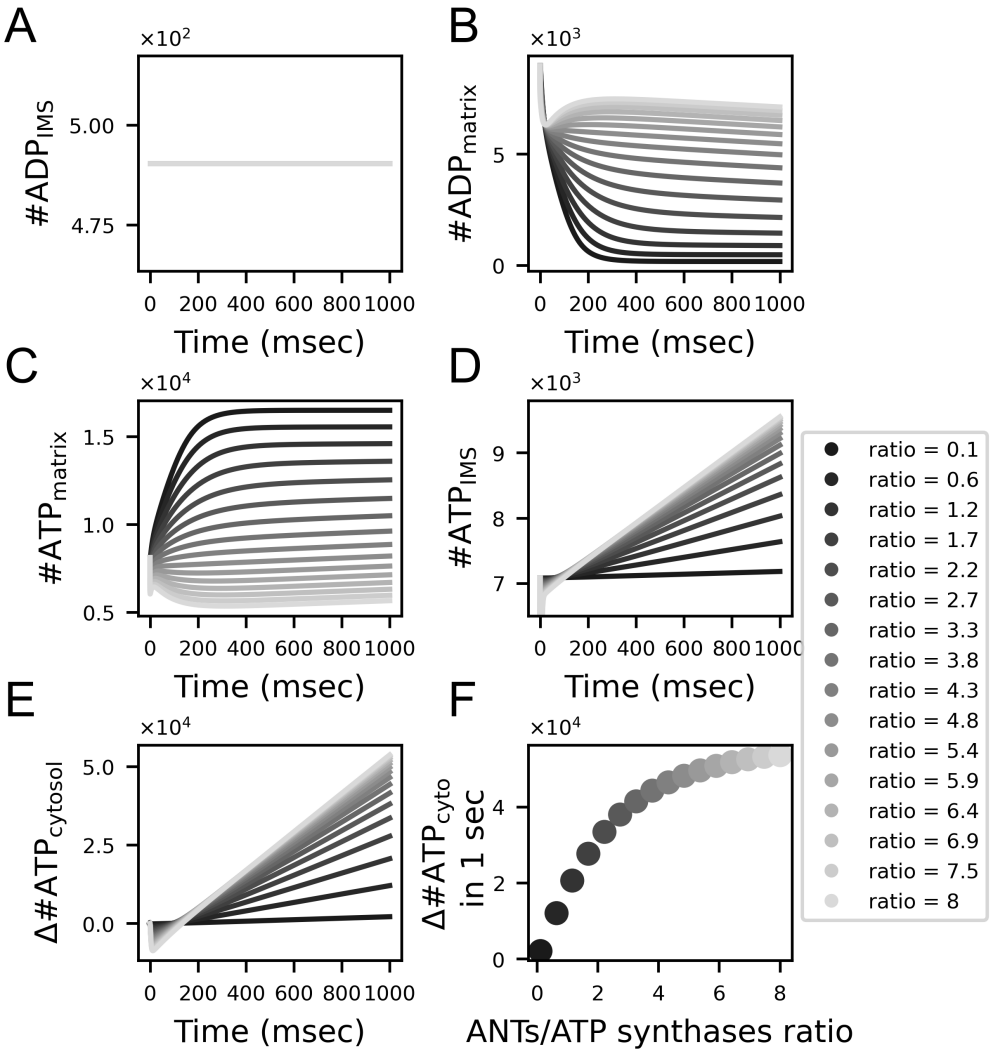

FIGURE 8. What is the limiting factor, export through ANTs or production of ATP through ATP synthases? We changed the ratio of ANTs to ATP synthases to answer this question. (A) Number of ADP molecules measured over time in the IMS. (B) Number of ADP molecules measured in the matrix. (C) Number of ATP molecules in the matrix. (D) Number of ATP molecules IMS. (E) Number of ATP molecules measured over time in the cytosol relative to the initial number. (F) Number of ATP molecules in the cytosol after 1 second relative to the initial concentration, for different ratios of ANT/ATP synthases. Ratios go from 0.1 to 8, the number of ATP synthases is kept constant and the number of ANTs increases (fast ANTs were considered r = 10).

reconstruction only the volume of the IMS decreases, due to the fact that the outer leaflet of OM was traced as well as the inner leaflet of the IM. Thus, the total volume encapsulated by the OM (V_{EOM}) and the matrix (V_{MA}) are constant in both cases (Table 8).

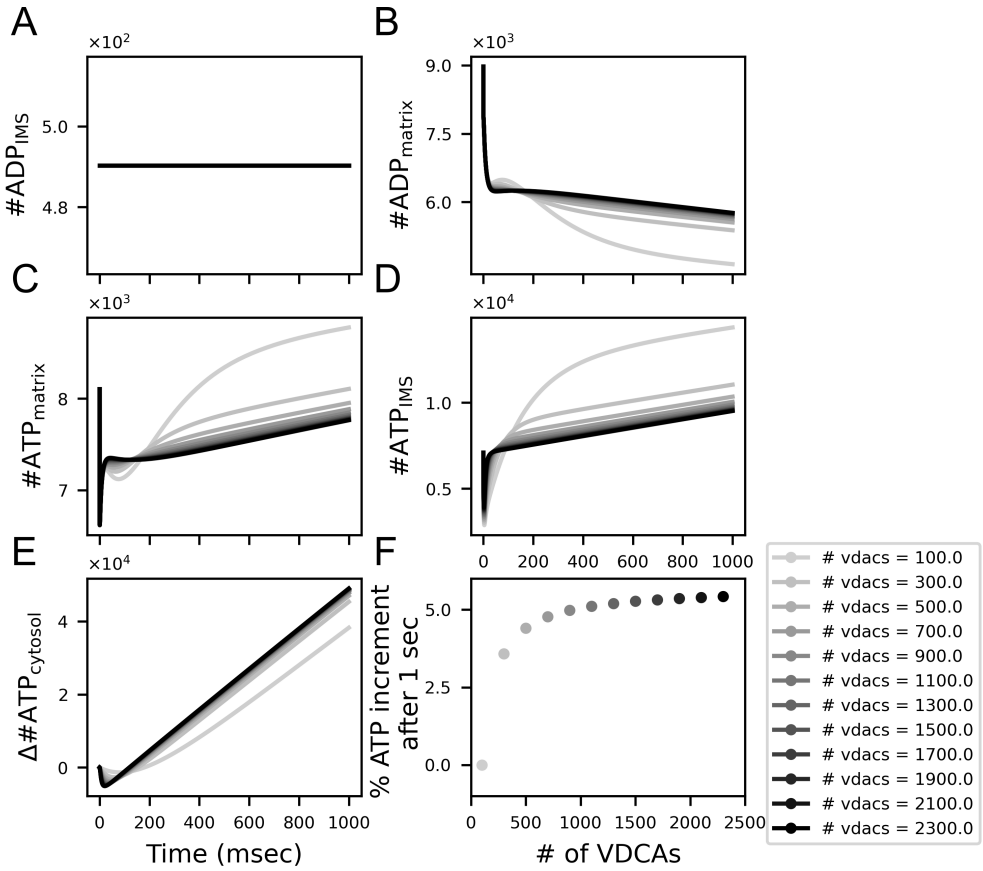

FIGURE 9. Effect of the number of VDACs on ATP efflux to the cytosol. (A) Number of ADP molecules measured over time in the IMS. (B) Number of ADP molecules measured over time in the matrix. (C) Number of ATP molecules measured over time in the matrix. (D) Number of ATP molecules measured over time in the IMS. (E) Number of ATP molecules measured over time in the cytosol relative to the initial concentration. (F) Percentage increase of ATP in the cytosol after 1 second for different numbers of VDACs in the OM. The number of VDACs goes from 100 to 2300 (in these simulations fast ANTs were considered, r = 10).

While the volume of the IMS is reduced to 11% of the total volume, and the volume of the membranes accounts for 10 % for the volume of the OM (V_{OM}) and 26% for the IM (V_{IM}). Thus, we find that in the case of mitochondria, volume information should include the effect of the membrane thickness as well.

4.4. **The compression of the IMS speeds up reactions and makes more ATP available in the cytosol.** The compression of the IMS has implications for the chemical reactions that happen in this compartment. We reanalyze our model with a compressed IMS. We observe an increase in the amount of ATP in the cytosol due to the compression of the IMS. This is because the compression accelerates the reactions in the IMS, importing

more ADP into the matrix and also exporting ATP at a higher velocity (Figure 10B-C). Similarly, the export through VDACs happens at a higher rate due to the compression (Figure 10D), which translates into more ATP in the cytosol (Figure 10F). 6% more ATP is found in the cytosol due to the compression of the IMS.

TABLE 8. Compression of the IMS due to membrane thickness. Relative and absolute volumes of all the membranes and compartments considering membrane thickness.

Membrane thickness (nm)	V_{EOM} (μm^3)	V_{OM} (μm^3)	V_{IM} (μm^3)	V_{IMS} (μm^3)	V_{MA} (μm^3)
0	0.0388	0	0	0.0181 (47 %)	0.0207 (53 %)
7	0.0388	0.004 (10 %)	0.0097 (26 %)	0.0044 (11 %)	0.0207 (53 %)

5. DISCUSSION

Given the indispensable nature of mitochondria in cellular energy production, having accurate models of mitochondrial dynamics are critical for understanding their impact on cellular function. In this work, we focused on developing a thermodynamically-consistent model of ATP production in mitochondria to ensure that the model is physically-plausible. In doing so, we derived the relationships for the dependence of kinetic parameters on the membrane potential, proton and substrates concentration.

We explored different parameter regimes to understand in which conditions ATP production or its export are a limiting step in making ATP available in the cytosol. We found that when the ratio of ANTs to ATP synthases is smaller than two, the export of ATP molecules is limited by ANTs, but having more than two times the number of ATP synthases makes ATP production the limiting step. This is in accordance with experimental observations [22]. Similarly, the number of VDACs do not limit the export of ATP, unless there are few VDACs present (in the order of 100's, for the ratio of ANTs/ATP synthases considered).

Finally, we analyzed the portion of the total volume taken up by the membranes and studied the functional effect this can have on the availability of ATP in the cytosol. The inner membrane takes up an estimate of 26 % of the volume enclosed by the OM, while the OM only takes up 10 % of this volume. The matrix and the IMS take up 53 % and 11 % respectively. The compression of the IMS produced by considering the membrane thickness has implications for the availability of ATP in the cytosol. After 1 second, 6 % more ATP is found due to the compression of the IMS; the reduction of this volume speeds up the reactions that occur inside this compartment, generating faster import of ADP to the matrix and faster export of ATP from the IMS.

Our findings have implications for understanding experimental observations. Different functional states have been characterized in isolated mitochondria [25, 26]. In particular an active state, referred in the literature as state 3, presents a compressed matrix. It is possible that like the compression of the IMS, the compression of the matrix could have

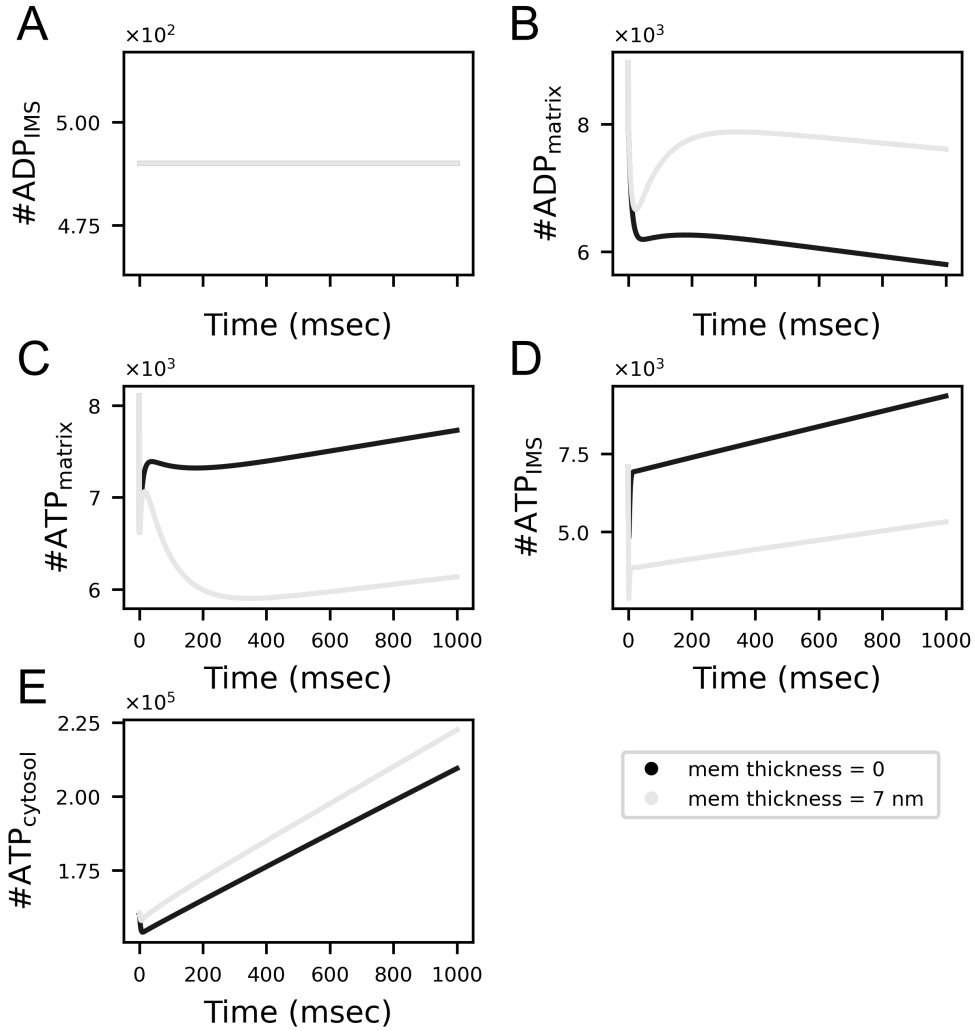

FIGURE 10. Functional consequences of the compression of the IMS. Simulations were performed assuming a membrane thickness of 7 nm (in gray) and zero (in black). (A) The amount of ADP molecules is the same in all conditions. (B) Number of ADP molecules over time in the matrix. (C) Number of ATP molecules over time in the matrix. (D) Number of ATP molecules over time in the IMS. (E) Number of ATP molecules over time in the cytosol.

functional implications. In our simulations a matrix compression of 50 % generates an increment of 2 % of ATP after 1 second (Supplementary Figure 6).

Additionally, we built the model in compartmental BioNetGen [20], and conducted non-spatial stochastic simulations. For the amount of ATP synthases and ANTs considered in this work, no stochastic effects were evident (Supplementary Figure 4), only reducing the number of ATP synthases in the orders of 100s stochastic effects are appreciable (Supplementary Figure 5). Future efforts will likely involve simulations in spatially resolved geometries of mitochondria including realistic geometries [4, 27]. Thus, our model lays

the foundation for future studies of the internal mitochondrial physiology and metabolism in cellular physiology.

6. ACKNOWLEDGMENTS

This work was supported by Air Force Office of Scientific Research (AFOSR) Multidisciplinary University Research Initiative (MURI) grant FA9550-18-1-0051 (to P. Rangamani).

REFERENCES

[1] D. Pietrobon and S. R. Caplan. Flow-force relationships for a six-state proton pump model: Intrinsic uncoupling, kinetic equivalence of input and output forces, and domain of approximate linearity. *Biochemistry*, 24(21):5764–5776, 1985.

[2] G. Magnus and J. Keizer. Minimal model of beta-cell mitochondrial Ca^{2+} handling. *American Journal of Physiology-Cell*, 273:C717 – C733, 1997.

[3] E. Metelkin, I. Goryanin, and O. Demin. Mathematical modeling of mitochondrial adenine nucleotide translocase. *Biophysical Journal*, 90(2):423–432, 2006.

[4] G. C. Garcia, T. M. Bartol, S. Phan, E. A. Bushong, G. Perkins, T. J. Sejnowski, M. H. Ellisman, and A. Skupin. Mitochondrial morphology provides a mechanism for energy buffering at synapses. *Scientific reports*, 9, 2019.

[5] B. Alberts, K. Roberts, J. Lewis, D. Bray, K. Hopkin, A. D. Johnson, P. Walter, and M. Raff. *Essential cell biology*. Garland Science, 2015.

[6] M. Yoshida, E. Muneyuki, and T. Hisabori. Atp synthase-a marvellous rotary engine of the cell. *Nature reviews Molecular cell biology*, 2(9):669, 2001.

[7] M. Colombini. Vdac: the channel at the interface between mitochondria and the cytosol. *Molecular and cellular biochemistry*, 256(1):107–115, 2004.

[8] S. Cortassa, M. A. Aon, E. Marban, R. L. Winslow, and B. O'Rourke. An integrated model of cardiac mitochondrial energy metabolism and calcium dynamics. *Biophysical Journal*, 84:2734–2755, 2003.

[9] M.-H. T. Nguyen, S. J. Dudycha, and M. S. Jafri. Effect of ca2+ on cardiac mitochondrial energy production is modulated by na+ and h+ dynamics. *American Journal of Physiology-Cell Physiology*, 292(6):C2004–C2020, 2007.

[10] R. Bertram, M. Gram Pedersen, D. S. Luciani, and A. Sherman. A simplified model for mitochondrial atp production. *Journal of Theoretical Biology*, 243(4):575–586, 2006.

[11] G. Magnus. *A mitochondria-based model for bursting and its D-glucose dependence in the pancreatic beta cell*. University of California, Davis, 1995.

[12] B. Thomas. A model of mitochondrial calcium induced calcium release. *Doctoral dissertation The Ohio State University*, 2007.

[13] T. L. Hill. *Free energy transduction in Biology. The steady-state kinetic and thermodynamic formalism*. Academic Press, 1977.

[14] S. R. Caplan and A. Essig. *Bioenergetics and linear nonequilibrium thermodynamics*. Harvard University Press, 1983.

[15] S. Caplan. Reciprocity or near-reciprocity of highly coupled enzymatic processes at the multidimensional inflection point. *Proc. Natl Acad. Sci. USA*, 78(7):4314–4318, 1981.

[16] J. P. Keener and J. Sneyd. *Mathematical physiology*, volume 1. Springer, 1998.

[17] R. Kraemer and M. Klingenberg. Electrophoretic control of reconstituted adenine nucleotide translocation. *Biochemistry*, 21(5):1082–1089, 1982.

[18] C. Duyckaerts, C. M. Sluse-Goffart, J. P. Fux, F. E. Sluse, and C. Lièbecq. Kinetic mechanism of the exchanges catalysed by the adenine-nucleotide carrier. *European Journal of Biochemistry*, 106(1):1–6, 1980.

[19] R. H. Clewley, W. E. Sherwood, M. D. LaMar, and J. M. Guckenheimer. PyDSTool, a software environment for dynamical systems modeling, 2007.

[20] L. A. Harris, J. S. Hogg, J.-J. Tapia, J. A. P. Sekar, S. Gupta, I. Korsunsky, A. Arora, D. Barua, R. P. Sheehan, and J. R. Faeder. BioNetGen 2.2: advances in rule-based modeling. *Bioinformatics*, 32(21):3366–3368, 2016.

[21] T. Gropp, N. Brustovetsky, M. Klingenberg, V. Müller, K. Fendler, and E. Bamberg. Kinetics of electrogenic transport by the ADP/ATP carrier. *Biophysical Journal*, 77(2):714–726, 1999.

[22] P. Vignais, P. Vignais, and J. Doussiere. Functional relationship between the adp/atp-carrier and the f1-atpase in mitochondria. *Biochimica et Biophysica Acta (BBA)-Bioenergetics*, 376(2):219–230, 1975.

[23] V. De Pinto, O. Ludwig, J. Krause, R. Benz, and F. Palmieri. Porin pores of mitochondrial outer membranes from high and low eukaryotic cells: biochemical and biophysical characterization. *Biochimica et Biophysica Acta (BBA) - Bioenergetics*, 894(2):109–119, 1987.

[24] G. Perkins, C. Renken, M. Martone, S. Young, M. Ellisman, and T. Frey. Electron tomography of neuronal mitochondria: three-dimensional structure and organization of cristae and membrane contacts. *Journal of structural biology*, 119(3):260–272, 1997.

[25] C. R. Hackenbrock. Ultrastructural bases for metabolically linked mechanical activity in mitochondria. I. reversible ultrastructural changes with change in metabolic steady state in isolated liver mitochondria. *The Journal of Cell Biology*, 30(2):269–297, 1966.

[26] C. R. Hackenbrock. Ultrastructural bases for metabolically linked mechanical activity in mitochondria. II. Electron transport-linked ultrastructural transformations in mitochondria. *The Journal of Cell Biology*, 37(2):345, 1968.

[27] R. Mendelsohn, G. C. Garcia, T. M. Bartol, C. T. Lee, P. Khandelwal, E. Liu, D. J. Spencer, A. Husar, E. A. Bushong, S. Phan, G. Perkins, M. H. Ellisman, A. Skupin, T. J. Sejnowski, and P. Rangamani. Morphological principles of neuronal mitochondria. *Journal of Comparative Neurology*, 2021.